Electrical Power and Energy Systems 131 (2021) 107070

Contents lists available at ScienceDirect

International Journal of Electrical Power and Energy Systems

journal homepage: www.elsevier.com/locate/ijepes

A multi-terminal traveling wave fault location method for active distribution network based on residual clustering

Jian Qiao, Xianggen Yin, Yikai Wang *, Wen Xu, Liming Tan

State Key Laboratory of Advanced Electromagnetic Engineering and Technology, Huazhong University of Science and Technology, 430074 Wuhan, China

ARTICLE INFO

Keywords:
Fault location
Traveling wave
Residual clustering
Active distribution network

ABSTRACT

Since distribution networks have multiple branches, complex topologies and increasing penetration of the distributed energy resources (DERs), the accurate fault location is difficult to realize. The existing traveling wave fault location methods are strongly affected by the arrival time errors. To overcome the problems mentioned above, a multi-terminal traveling wave fault location method is proposed for active distribution networks based on residual clustering. Firstly, the traveling wave arrival times are utilized to construct a minimized optimization model for each section. The objective optimization function represents the minimization of the sum of squared errors (MSSE), and the global optimal solutions reflect the wave velocity and the fault distance. Subsequently, the particle swarm optimization algorithm (PSO) is used to solve the above optimization models, and the section with the minimum MSSE is judged as the faulty section. Finally, the density-based spatial clustering of applications with noise (DBSCAN) algorithm is utilized to group the residuals of the faulty section to identify the bad data, which are affected by the arrival time errors. And the normal data remained are applied to reconstruct the optimization model and calculate the optimal solution of the fault distance. Thus, the fault location results can be corrected. Simulation results and field tests indicate that the proposed method has high fault location accuracy, strong robustness to time errors and high adaptability for active distribution networks.

1. Introduction

Rapid and accurate fault location for distribution networks can effectively accelerate fault maintenance and power supply recovery, which is of great significance to improve the system stability and reliability. In recent years, distribution systems around the world have gradually commercialized the use of DERs, including photovoltaic solar energy, wind energy and battery energy, etc. [1]. With the large-scale integration of DERs and its associated power electronics, the "radial" structure and passive characteristic of traditional distribution networks have disappeared. Meanwhile, the power flow direction of some feeders in the grid has changed from unidirectional to bidirectional and the fault characteristics are quite different from traditional system, which result in the false coordination with the conventional over-current protection. Thus, the protection and fault location performance become urgently to be enhanced [2–3].

If the primary equipment is not added, the existing accurate fault location methods can be broadly classified into two main categories based on the utilized principle: impedance-based methods and traveling wave-based methods. Impedance-based methods are easily affected by network structure, line parameters, CT saturation and unbalanced three-phase loads, and the location accuracy is low [4–7]. In addition, the distributed generations (DGs) based on inverter usually have fault ride-through ability, which adversely affects the impedance-based methods. However, traveling wave-based methods are not affected by fault conditions, CT saturation and load conditions [8–12], which have high location accuracy and obviously theoretical advantages. With the development of PMU device, wireless communication and signal processing technology [13], traveling wave-based methods have shown great application potential. More importantly, the traveling wave-based methods have excellent adaptability to DERs. On the one hand, the length of distribution lines is generally short, thus the initial traveling wave can be caught in dozens of microseconds (μs). While the control response time (the control time and the switching time of control strategy) of distributed generations is milliseconds (ms). The initial traveling wave will reach the measuring point earlier than power electronic devices control response. Thus, the traveling wave-based method can be free from the influence of DERs. On the other hand, traveling

* Corresponding author.
E-mail address: 742657004@qq.com (Y. Wang).

https://doi.org/10.1016/j.ijepes.2021.107070
Received 15 December 2020; Received in revised form 28 February 2021; Accepted 2 April 2021
Available online 16 April 2021

wave is essentially a transmission state of electromagnetic wave on transmission line. The initial traveling wave is only related to the superimposed fault voltage source and the distributed parameters of the line. Therefore, DERs can be regarded as the boundary of the line, which have a certain impact on the subsequent refraction and reflection of the traveling wave, while the initial traveling wave will not be affected.

Distribution networks have a multilayer branch structure with short lines. Hence, the mature two-ended traveling wave method in the transmission networks is difficult to be directly adopted [14]. Currently, the theoretical research of the traveling wave-based method in the distribution networks focuses on the use of multi-terminal measurement information [15–26]. In [15], a set of linear equations are constructed with the arrival times at all nodes, and the faulty section is obtained by solving the equations. However, the location result of this method is susceptible to the error of wave velocity. In [16,17], a fault distance difference matrix is constructed by using the arrival times of the fault-generated traveling wave, through comparing the matrix elements with those in the topological distance difference matrix, the faulty section and fault location can be realized. In [18,19], a set of fault distances are calculated based on the principle of the two-ended traveling wave, and the fault distances are compared with the branch length to determine the faulty branch. The method in [20] analyses the characteristics of the arrival time differences of the initial traveling waves in different faulty sections, and utilizes these characteristics to identify the reflected traveling wave of the fault point, then the fault distance can be calculated based on the signal-ended method. However, the above methods in [16–20] depend on the accuracy of time information. When there are time errors, it may misjudge the faulty section and cause the location failure. In addition, the method in [20] depends on the accurate identification of reflected traveling wave, while the fault traveling wave can be reflected at the wave impedance discontinuities such as branch points and network terminals. Thus, it is extremely difficult to identify the reflected traveling wave of the fault point, which makes it difficult to apply the single-ended method in the distribution networks [20–23]. In [24,25], the location criterion is constructed for every possible fault point in the network based on the arrival time differences of the traveling waves, which is not necessary to identify the faulty section in advance. However, each potential fault point is obtained by one simulation process, which aggravates the calculation of fault location. In [26], redundant fault location equations are constructed by using the traveling wave information of multiple measuring points, then the multiple initial fault distances are solved. Finally, the weighted average method is used to fuse the fault distances. However, the fusion effect of this method is easily affected by the weight setting. The methods in [24–26] utilize the redundant time information for fault location, they have a certain degree of time error tolerance, but cannot avoid the effect of time error on location results. When several detectors have large time errors, the fault location may be failed.

In view of the defects of the above methods, a multi-terminal traveling wave fault location method for active distribution network based on residual clustering is proposed in this paper. When a fault occurs, the initial traveling wave arrival times are utilized to construct the minimized optimization model for all sections respectively, where the objective function represents the MSSE and the optimal solutions reflect the traveling wave velocity and the fault distance. Then, PSO algorithm is utilized to solve the optimization model of each section. The section with the minimum MSSE is judged as the faulty section, and the corresponding optimal solutions are the initial solution of traveling wave velocity and fault distance. In order to reduce the effect of time errors on the location result, DBSCAN algorithm is utilized to group the residuals of the faulty section and identify the bad data which are affected by time errors. The optimization model is repeatedly constructed by using the remained normal data. Then the corrected solution of the fault distance is calculated to obtain the real fault location result. Simulation results and field tests show that the proposed method has high accuracy and strong robustness to time errors.

2. The fault location method based on multi-terminal traveling wave

At present, the methods for traveling wave detection are relatively mature, including wavelet transform [27], Hilbert-Huang transform (HHT) [28], S-transform [29,30], teager energy operator (TEO) [31] and mathematical morphology (MM) [32], etc. Among them, S-transform has the advantage of extracting the traveling wave with a specific frequency. Since the velocity of the aerial-mode traveling wave is closely related to frequency, if a specific frequency of the aerial-mode traveling waves and their arrival times can be extracted, the traveling wave velocity in the network can be considered as a constant. According to the Nyquist sampling theorem, if the original signal with frequency f is recovered from the sampling signal without distortion, the sampling frequency should be greater than $2f$. Therefore, the Nyquist frequency is $0.5\,f_s$ when the sampling rate of the traveling wave detector is f_s. In this paper, generalized S-transform [33] is utilized to detect the arrival times of aerial-mode traveling waves at Nyquist frequency.

Before fault location, the network topology is defined as follows. Ignore primary equipment such as main power supply, transformer and circuit breaker. The terminals of the network are defined as the endpoints, denoted as “D”; the line intersections are defined as the branch points, denoted as “B”. In this paper, D-PMU device is used to detect the traveling wave signal of aerial-mode voltage [34,35]. Due to the high cost of D-PMU and the limited space and load-bearing capacity of the overhead wire tower, most branch points have no conditions for additional installation of D-PMU. Therefore, this paper only places D-PMUs at the endpoints.

Take the complex radiant distribution network shown in Fig. 1 as an example. The network structure of its equivalent transformation is shown in Fig. 2, according to the definition of the above network topology. Fig. 2 shows a total of 16 endpoints, 12 branch points, and the node corresponding relationship between Fig. 1 and Fig. 2 is shown in Table 1. 16 D-PMUs are installed in this network, and the symbol of each detector is the same as the corresponding endpoint, denoted as “$D_1 \sim D_{16}$”; The arrival times of the measured initial traveling waves are denoted as “$T_1 \sim T_{16}$”.

The premise of accurate fault location is identifying the faulty section. Both the endpoint “D” and branch point “B” in. Fig. 2 are considered as node “N”, any two nearest nodes constitute a section. There are 27 sections in total without line overlap. For a section N_iN_j composed of adjacent nodes N_i and N_j, the network can be divided into two parts. The upstream part is directly connected to the node N_i, and the downstream part is directly connected to the node N_j. The D-PMU detectors are also divided into two groups. The detectors contained in the upstream part

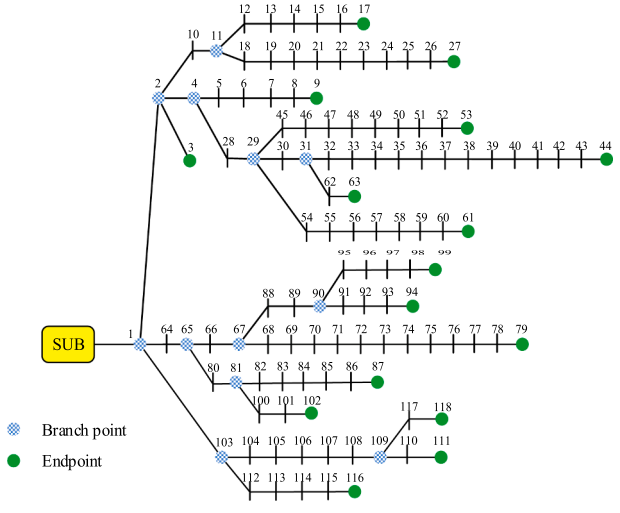

Fig. 1. Complex radiant distribution network.

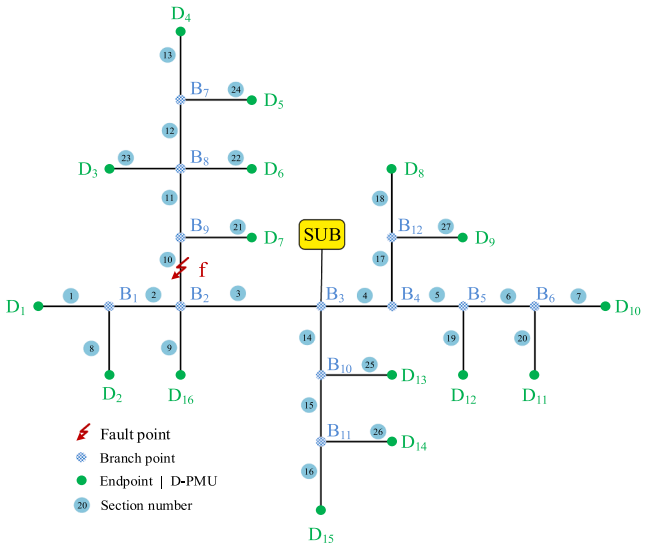

Fig. 2. Equivalent network after transformation.

Table 1
The node corresponding relationship between Fig. 1 and Fig. 2.

Fig. 1	Fig. 2	Fig. 1	Fig. 2	Fig. 1	Fig. 2	Fig. 1	Fig. 2
D_1	17	D_8	87	D_{15}	118	B_6	90
D_2	27	D_9	102	D_{16}	3	B_7	31
D_3	53	D_{10}	99	B_1	11	B_8	29
D_4	44	D_{11}	94	B_2	2	B_9	4
D_5	63	D_{12}	79	B_3	1	B_{10}	103
D_6	61	D_{13}	116	B_4	65	B_{11}	109
D_7	9	D_{14}	111	B_5	67	B_{12}	81

are denoted as the set S_u. The detectors contained in the downstream part are denoted as the set S_d. The optimization model is constructed according to the known line lengths and the measured traveling wave arrival times. The objective function and constraint conditions are as follows:

$$\begin{cases} min \quad f_{N_iN_j}(v,l) = \sum^{C(n,2)} R_{xy}^2 \\ \qquad R_{xy} = L_{N_jD_x} - L_{N_jD_y} - v\ (T_x - T_y) - 2\ l\ d_{xy} \\ \qquad d_{xy} = 1 \qquad D_x \in S_u\ ,\ D_y \in S_d \\ \qquad d_{xy} = 0 \qquad D_x,\ D_y \in S_u \ \text{ or } \ D_x,\ D_y \in S_d \\ \qquad \text{s.t.} \qquad 0 < v < v_c \\ \qquad\qquad 0 \leqslant l \leqslant L_{N_iN_j} \end{cases} \tag{1}$$

Where $L_{N_jD_x}$ and $L_{N_jD_y}$ are the line lengths from node N_j to detectors D_x and D_y respectively, T_x and T_y are the arrival times of traveling waves measured by detectors D_x and D_y respectively, n is the number of detectors, C(n, 2) is the number of combinations of any two detectors, i.e. $n(n\text{-}1)/2$, d_{xy} is a 0–1 coefficient related to the position of the detectors, v_c represents the speed of light, $L_{N_iN_j}$ represents the line length of section N_iN_j. In mathematical statistics, residual refers to the difference between the actual observed value and the estimated value, which can be regarded as the observed value of the error. When the estimated value is equal to the actual observed value, the residual is zero. In this paper, $L_{N_jD_x} - L_{N_jD_y}$ is regarded as the actual observed value, $v\ (T_x - T_y) + 2l\ d_{xy}$ is regarded as the estimated value based on the decision variables [v, l]. On this basis, R_{xy} can be regarded as the residual, and the objective function $f_{N_iN_j}$ can be regarded as the MSSE of the section N_iN_j. The optimal solution of the decision variable v represents the wave velocity, and the optimal solution of the decision variable l represents the line length between the fault f and the downstream node N_j.

PSO algorithm is used to solve the above optimization model [36]. The relevant parameters are set as follows: the total number of particles is 5, the dimension of each particle is 2 which represent the wave velocity and the fault distance respectively. The velocity thresholds of particles are $\pm$ 0.03v_c and $\pm$ 10 respectively. The learning factors are 1.5, and the inertia weight decreases nonlinearly from 0.5695 to 0.1565. Since Eq. (1) is a convex optimization problem, its local optimal value must be the global optimal value. Therefore, few iterations can converge to the optimal solution. In this paper, the number of iterations is set as 100, the algorithm will terminate when the number of iterations exceeds 100.

Obviously, each section can build a similar optimization model. The fault f in Fig. 2 is located on section B_9B_2. When the section N_iN_j is exactly the faulty section B_9B_2, the network divided result is shown in Fig. 3, where S_u contains detectors {D_3, D_4, D_5, D_6, D_7}, S_d contains detectors {D_1, D_2, D_8, D_9, D_{10}, D_{11}, D_{12}, D_{13}, D_{14}, D_{15}, D_{16}}. Eq. (1) can be rewritten as:

$$\begin{cases} min \quad f_{B_9B_2}(v,l) = \sum^{C(16,2)} R_{xy}^2 \\ \qquad R_{xy} = L_{B_2D_x} - L_{B_2D_y} - v\ (T_x - T_y) - 2l\ d_{xy} \\ \qquad d_{xy} = 1 \qquad D_x \in S_u\ ,\ D_y \in S_d \\ \qquad d_{xy} = 0 \qquad D_x,\ D_y \in S_u \ \text{ or } \ D_x,\ D_y \in S_d \\ \qquad \text{s.t.} \qquad 0 < v < v_c \\ \qquad\qquad 0 \leqslant l \leqslant L_{B_9B_2} \end{cases} \tag{2}$$

When there are no time errors, the global optimal solutions of decision variables [v, l] are:

$$\begin{cases} v = v_{wave} \\ l = l_{fB_2} \end{cases} \tag{3}$$

Where v_{wave} is the ideal wave velocity, and l_{fB_2} is the distance between the fault f and the downstream node B_2. It can be analysed that all the C(16,2) coefficients R_{xy} are 0 and the minimum value of the objective function is 0 by substituting the results of Eq. (3) into Eq. (2). Therefore, when there are no time errors, the MSSE of the faulty section is 0, and the optimal solutions of the decision variables are the real traveling wave velocity and fault distance.

When the section N_iN_j is a non-fault section, take section B_8B_9 as an

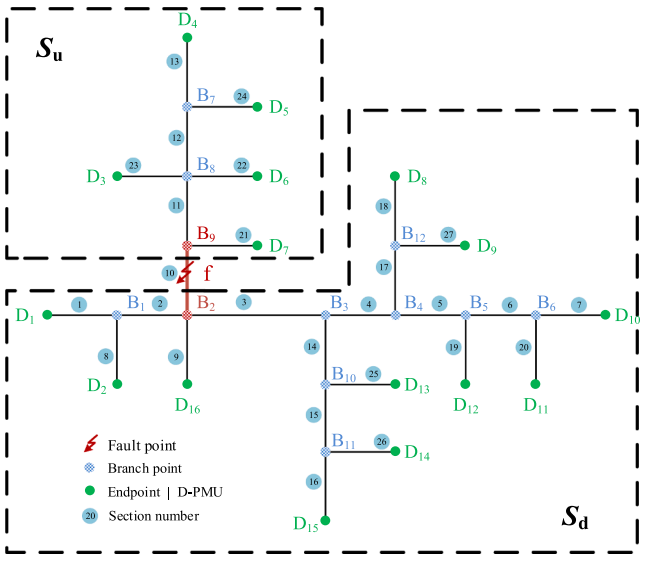

Fig. 3. The network divided result of the faulty section B_9B_2.

example to explain. The network divided result is shown in Fig. 4, where $\boldsymbol{S_u}$ contains detectors {D_3, D_4, D_5, D_6}, $\boldsymbol{S_d}$ contains detectors {D_1, D_2, D_7, D_8, D_9, D_{10}, D_{11}, D_{12}, D_{13}, D_{14}, D_{15}, D_{16}}. Eq. (1) can be rewritten as:

$$\begin{cases} min \quad f_{B_8B_9}(v,l) = \sum^{C(16,2)} R_{xy}^2 \\ \qquad R_{xy} = L_{B_9D_x} - L_{B_9D_y} - v\ (T_x - T_y) - 2l\ d_{xy} \\ \qquad d_{xy} = 1 \qquad D_x \in \boldsymbol{S_u}\ , \quad D_y \in \boldsymbol{S_d} \\ \qquad d_{xy} = 0 \qquad D_x,\ D_y \in \boldsymbol{S_u} \quad or \quad D_x,\ D_y \in \boldsymbol{S_d} \\ \qquad s.t. \qquad 0 < v < v_c \\ \qquad\qquad\qquad 0 \leqslant l \leqslant L_{B_8B_9} \end{cases} \tag{4}$$

It can be seen that detector D_7 is located in upstream of the fault, but it is grouped into the downstream set $\boldsymbol{S_d}$, which makes the solution of the optimization model more complicated. When there are no time errors, the C(16,2) combinations of detectors for section B_8B_9 are discussed in three cases for the convenience of analysis.

Case 1: If detector D_7 is ignored, there are a total of C(15,2) combinations of detectors to construct a sub-optimization model by using the remained detectors. The optimal solutions with MSSE equal to 0 exist in this sub-optimization model, when the constraint conditions are not considered:

$$\begin{cases} v_{case1} = v_{wave} \\ l_{case1} = -l_{f\ B_9} \end{cases} \tag{5}$$

Case 2: When one detector is D_7 and the other detector belongs to $\boldsymbol{S_u}$, there are 4 detector combinations and d_{xy} is equal to 1. The sub-optimization model in this case has the optimal solutions with MSSE equal to 0:

$$\begin{cases} v_{case2} = v_{wave} \\ l_{case2} = 0 \end{cases} \tag{6}$$

Case 3: When one detector is D_7 and the other detector belongs to $\boldsymbol{S_d}$, there are 11 detector combinations and d_{xy} is equal to 0. The sub-optimization model in this case has no optimal solutions with MSSE equal to 0. For each combination, the solutions with residual equal to 0 are different and may not satisfy the constraint conditions, as shown in Eq. (7).

$$v_{case3.D_7D_i} = \left(1 - \frac{2l_{f\ B_9}}{l_{f\ D_7} - l_{f\ D_i}}\right) \quad v_{wave} \qquad D_i \in \boldsymbol{S_d} \tag{7}$$

Compared with Eq. (5)-(7), when the fault is not at branch point B_9, the solutions of the three cases are different and may not satisfy the constraints. Thus, the MSSE of B_8B_9 is much greater than 0. In addition, the network divided results of each section are unique and different from each other. Therefore, at least one detector is wrongly grouped in the network divided result of the non-fault section. It can be inferred that the other non-fault sections are similar to section B_8B_9, whose MSSE are also much greater than 0. On this basis, the MSSE of all sections are calculated and the section with the minimum calculated value is selected as the faulty section, which is expressed as:

$$f_{MN}(v,l) = \min\{\quad f_{D_1B_1}, f_{B_1B_2} \quad \dots \quad , f_{B_8B_9}, f_{B_9B_2}, \quad \dots \quad \} \tag{8}$$

Where section MN is the faulty section, the optimal solutions [v, l] are the initial solutions of wave velocity and fault distance, respectively.

This method is also applicable to the special case where the fault is just located at the branch point. When the fault is located at branch point B_9, sections B_8B_9, B_9B_2 and D_7B_9 are all faulty sections. If there are no time errors, the MSSE of these three sections above are 0.

In practical engineering, the MSSE of the faulty section will not be exactly equal to 0 due to the errors of the traveling wave arrival times, but it is still much smaller than that of non-fault sections. In addition, the traveling wave velocity is regarded as an unknown quantity when the faulty section is identified by the method in this paper, thus the judgment result of the faulty section is not affected by the error of wave velocity which has high reliability.

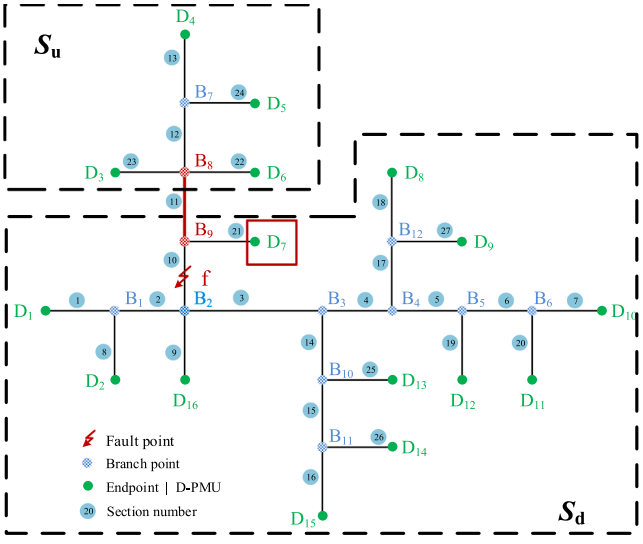

Fig. 4. The network divided result of the non-fault section B_8B_9.

3. The correction method based on residual clustering for fault location result

The wave velocity is close to the speed of light, and the arrival times of the initial traveling waves detected by each D-PMU are almost the same, hence a small-time error can also cause a large location error. Generally, the location error of the traveling wave-based method in transmission networks is less than 300 m which is also less than the distance between two towers. However, this error will greatly expand the scope of line patrol and even lead to fault location failure for the distribution networks. Therefore, the traveling wave location method in distribution networks should have a strong time error robustness. This paper proposes a correction method based on residual clustering for fault location result after Section 2.

For a distribution network with n D-PMUs. When $T_1 \sim T_n$ are the ideal traveling wave arrival times, the C(n,2) residuals of the faulty section are all 0 and the optimal solution of the decision variable l is the accurate fault distance. When there is a large time error in T_x or T_y, the absolute value of the residual R_{xy} will be much greater than 0, which belongs to the bad data. The absolute values of the remained residuals are close to 0, which belong to the normal data, all residuals form two distinct categories, namely two clusters. Therefore, the bad data affected by the time errors can be identified based on the absolute values of all residuals, and the influence of time errors on the location result can then be reduced. In this paper, DBSCAN algorithm is utilized to cluster the residuals of the faulty section to identify bad data.

Firstly, the C(n, 2) residuals of the faulty section are sorted and renumbered in absolute value from smallest to largest as the sample set $\boldsymbol{S_R}$:

$$\boldsymbol{S_R} = \{\quad R_1 \quad R_2 \quad \dots \quad R_q \quad \dots \quad R_{C(n,2)} \quad \} \tag{9}$$

DBSCAN is a clustering algorithm [37–39], which is based on the density of the samples, it can reliably cluster the samples and effectively deal with noise without setting the number of clusters in advance. Concretely, this algorithm utilizes parameters [*Eps*, *minPts*] to describe the density of the samples, where *Eps* is a threshold for the neighborhood distance, and *minPts* is a threshold for the number of *Eps*-neighborhood. The samples in the neighborhood of R_q are defined as a set, denoted as $\boldsymbol{S_{Eps.q}}$, $\boldsymbol{S_{Eps.q}} = \{R_p \in \boldsymbol{S_R} \quad : \quad |R_p - R_q| \leqslant Eps\}$. The number of the samples in $\boldsymbol{S_{Eps.q}}$ is defined as density, which is represented as $\rho(\boldsymbol{S_{Eps.q}})$.

If $\rho(S_{Eps.q}) \geqslant minPts$, the sample R_q is the core sample, R_p and R_q are directly density-reachable. If any two adjacent samples in sample R_1 $R_2 \ldots R_m$ are directly density-reachable, then any two samples of them are density-reachable. If the sample R_y and R_z are both density-reachable to the sample R_x, then R_y and R_z are density-connected, which is clearly symmetric. DBSCAN algorithm traverses the samples in $\boldsymbol{S_R}$. If a sample is detected as a core sample, then from the sample, it will start from this sample and expand to the density-reachable region to obtain a maximized cluster in which any two samples are density-connected. The clustering process ends when all clusters have no new samples added, and the samples that do not belong to any cluster are defined as noise, which are the bad data affected by the large time errors. According to the above definition, [*Eps*, *minPts*] parameters should be selected artificially before clustering. The traditional DBSCAN algorithm sets *minPts* to 4 and selects *Eps* by observation. However, the reliability of the observation method is extremely low. If the selected *Eps* is too small, the cluster of normal data will be divided into multiple clusters, and the ordinary samples will be misclassified into the noise. If the selected *Eps* is too large, part of the noise will be classified into the clusters by mistake. Therefore, this paper proposes an adaptive [*Eps*, *minPts*] parameters selection method based on the application background of the traveling wave location method.

In order to avoid the normal data being divided into multiple clusters, *minPts* should not be too large. Considering that there are C(*n*,2) samples in $\boldsymbol{S_R}$, the empirical value of *minPts* is:

$$minPts = \begin{cases} \lfloor (n-1)/2 \rfloor & n \geqslant 10 \\ 4 & 5 \leqslant n \leqslant 9 \end{cases} \tag{10}$$

Where is the least integer operator; *n* is the number of the D-PMU. Clustering algorithm is a data mining method based on big data. When the number of detectors is less than 5, there are fewer samples in $\boldsymbol{S_R}$ and the reliability of clustering result is low. On the contrary, the clustering result has higher reliability for the large distribution networks with a large number of detectors. Thus, the value of *minPts* for the distribution network shown in Fig. 2 is 7.

For the sample R_q, find the nearest *minPts* sample and record the distance between them as $dis_{minPts}(q)$. The distance set $\boldsymbol{S_{dis}}$ is obtained by traversing the samples in $\boldsymbol{S_R}$, $\boldsymbol{S_{dis}} = \{dis_{MinPts}(q) \quad : \quad R_q \in \boldsymbol{S_R}\}$. Take the distribution network shown in Fig. 2 as an example, when there are truncation time errors, the samples in $\boldsymbol{S_{dis}}$ are sorted in ascending order as shown in Fig. 5. The curve in the figure rises suddenly after a gentle part. Obviously, the ordinate of the mutation point is the ideal *Eps* to distinguish the normal data and bad data. Furthermore, this curve is highly similar to the J-H demagnetization curve after rotation [40], hence the empirical formula of *Eps* is obtained by referring to the definition of knee point, as shown in Eq. (11). In Fig. 5, the *Eps* calculated from Eq. (11) is approximately equal to the ordinate of mutation point. Therefore, the appropriate [*Eps*, *minPts*] parameters can be adaptively selected according to Eq. (10) and (11) without manual observation.

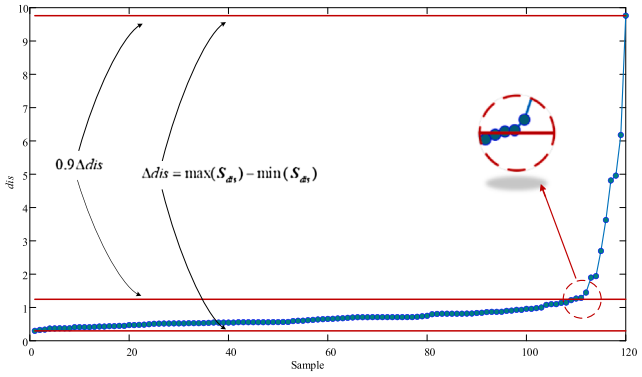

Fig. 5. The samples of $\boldsymbol{S_{dis}}$.

$$Eps = max \quad (\boldsymbol{S_{dis}}) - 0.9 \cdot [max(\boldsymbol{S_{dis}}) - min \quad (\boldsymbol{S_{dis}})] \tag{11}$$

Sample set $\boldsymbol{S_R}$ is clustered to obtain one or more clusters and noises based on the selected [*Eps*, *minPts*] parameters. The cluster with the smallest mean value in the clustering result is denoted as $\boldsymbol{S_H}$, and the samples in $\boldsymbol{S_H}$ are used to repeatedly construct the optimization model as shown in Eq. (12).

$$\begin{cases} min \quad f_{\mathrm{MN}}(v', l') = \sum^{H} |R_{xy}|^2 \\ \qquad\qquad |R_{xy}| \in \boldsymbol{S_H} \\ \text{s.t.} \qquad 0 < v' < v_{\mathrm{c}} \\ \qquad\qquad 0 \leqslant l' \leqslant L_{\mathrm{MN}} \end{cases} \tag{12}$$

Where H is the number of samples in $\boldsymbol{S_H}$, $[v', l']$ are the corrected solutions of the wave velocity and the fault distance.

In summary, the flow chart of the fault location method for active distribution network based on residual clustering is shown in Fig. 6.

4. Simulation and verification

4.1. Simulation model

Take the overhead-cable hybrid active distribution network shown in Fig. 7 as an example, the multi-terminal traveling wave fault location method based on residual clustering is simulated and verified. In the figure, the total length of the lines is 36.234 km, the length of overhead lines is 29.456 km and the length of cable lines is 6.778 km. The 27 sections in this network are numbered, and the length of each section is shown in the Appendix. 16 D-PMUs are placed at the network endpoints with a sampling rate of 10 MHz. PSCAD/EMTDC is used to establish the simulation model. The overhead lines adopt the frequency-dependent model, and the non-uniform transposition is set to simulate the asymmetry of line parameters. Gaussian noise with signal-to-noise ratio of 30 dB is added to the collected signals to simulate the effect of the noise during signal transmission. In order to eliminate the influence of the difference of wave velocity in the overhead-cable hybrid distribution network, this paper converts the hybrid distribution network into the equivalent overhead line distribution network by wave velocity conversion. The specific method is described in [41].

The DGs in Fig. 7 are all inverter-interfaced distributed generations (IIDGs), and the corresponding basic parameters are shown in Table 2. The control system includes active/reactive power separation outer loop control, low voltage ride through (LVRT) control and protection, and positive and negative sequence double current inner loop control, as shown in Fig. 8. The control strategy can suppress the negative sequence component of the output current and ensure the symmetry of the output current. It can also output different reactive power according to the voltage drop degrees at the point of common coupling (PCC) to support the system voltage.

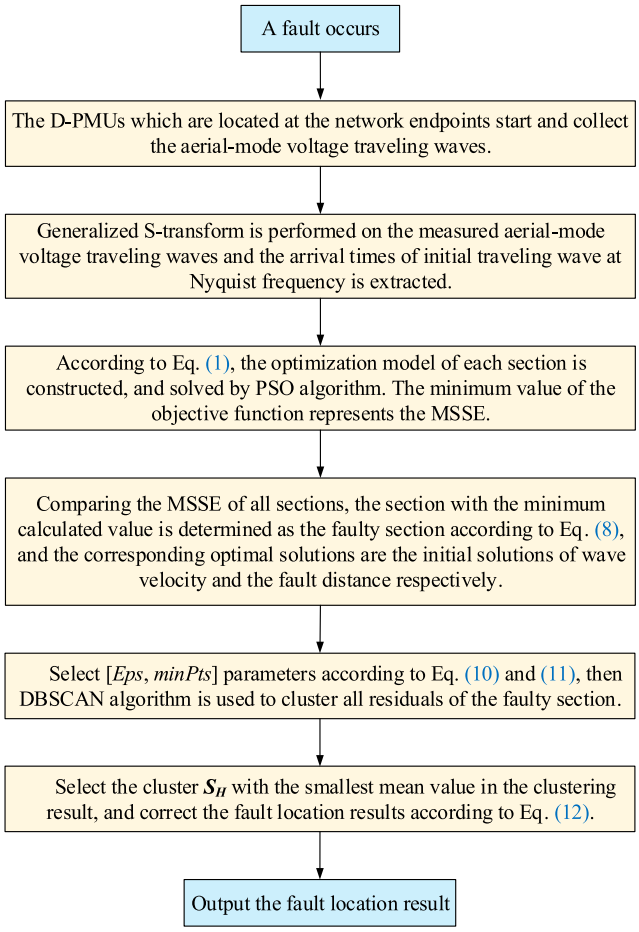

Fig. 6. The flow chart of the fault location method for active distribution network based on residual clustering.

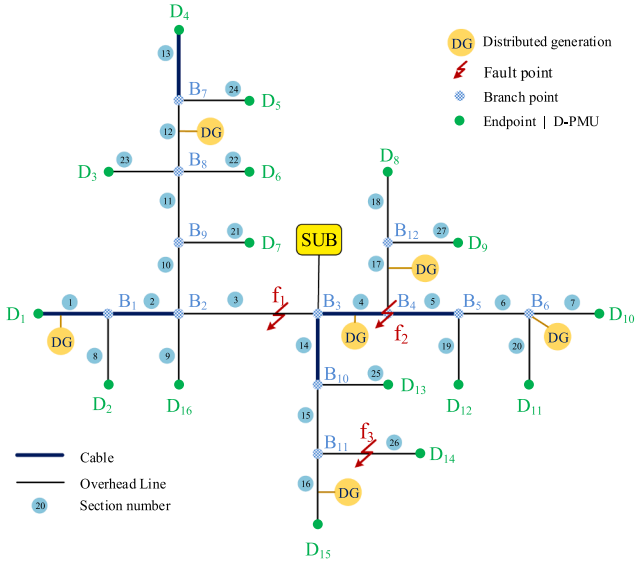

Fig. 7. Overhead-cable hybrid active distribution network.

4.2. The performance of the proposed method

The fault f_1 is located on section 3 (i.e. section B_2B_3) and is 1027 m away from the branch point B_3. Assume that the A-phase grounding fault occurs at f1 when the time is 0.1253 s, the fault inception angle is 60°, and the transition resistance is 500 Ω. Generalized S-transformation is applied to the aerial-mode voltage signals after phase-mode transformation. The results of generalized S-transformation and the arrival times of initial traveling waves are shown in Fig. 9 and Table 3 respectively. The fault f_2 is located at the branch point B4 (i.e. the intersection of section 4, 5 and 17), the fault f_3 is located on section 26 (i.e. section $B_{11}D_{14}$) which is only 100 m away from the branch point B_{11}. The initial traveling wave arrival times in case of fault f_2 or fault f_3 alone are shown in the Appendix.

Table 2
Basic parameters of the IIDG.

Parameter	Value	Parameter	Value
Effective value of output voltage (U_o/V)	690	DC bus voltage (U_{dc}/V)	800
Ratio of grid-connected transformer	0.69:10.5	Filter inductance (L_f/mH)	1
Switching frequency (f_s/kHz)	2	Filter capacitor (C_f/μF)	20
Grid frequency (f_g/Hz)	50	Proportional coefficient (k_p)	0.2
Power rating (P/MW)	2	Integral coefficient (k_i)	1000

When f_1, f_2 or f_3 occurs a fault separately, the MSSE of each section is calculated according to Eq. (1) and the arrival times of the initial traveling waves. Since the magnitude of the MSSE in non-fault sections are much larger than that in the faulty section. In order to facilitate the graphical display, the MSSE of each section is transformed into the gain form according to Eq. (13) on the premise of not changing the numerical characteristics. The results of faulty section identification are shown in Fig. 10. After the faulty section is identified accurately, the sample set S_R of the faulty section is clustered by DBSCAN based on the residual clustering method in Section 3. The clustering results of f_1, f_2 and f_3 are shown in Fig. 11. Finally, the fault location results are recorded in Table 4.

$$\begin{cases} f_{MN} = \min\{ f_1, f_2, \ldots, f_{27} \} \\ A_i = 20log(f_i/f_{MN}) \quad i \in [1,27] \end{cases} \tag{13}$$

For the fault f_1, the calculated value A_3 in Fig. 10 is 0 which is far less than that of other sections. Therefore, section 3 is accurately identified as the faulty section. The histogram and clustering result diagram of S_R are included in Fig. 11. The abscissa of the histogram reflects the absolute value of residuals, and the ordinate reflects the number of samples. The clustering result diagram is composed of one-dimensional scattered points, each of which corresponds to a sample. Its abscissa is also the absolute value of the residual, and there is no ordinate. The clustering result is represented by different colors. Where, the average value of Cluster 1 composed of red scattered points is the smallest, which represents the normal data, the green scattered points that do not belong to any cluster and are noise. The samples in Cluster 1 are extracted, then the corrected solutions $[v', l']$ are calculated according to Eq. (12). In Table 4, the location error of f_1 after correction is only 3.454 m with an error reduction of 64.31%. For the fault f_2, the calculated valuesA_4, A_5 and A_{17} are all small, where A_4 is the smallest. The f_2 is finally located on section 4 with an absolute error is only 5.784 m, which proves that this method can be applied to the case of branch point fault. It can be seen that the maximum location error of the three faults is only 6.836 m, which proves that the proposed method has high accuracy.

4.3. The performance of considering the time errors

In the actual system, the arrival times of traveling waves have synchronization error and detection error. The synchronization error depends on the clock accuracy of GPS, which is generally less than ± 1 μs. However, in extreme conditions such as GPS time synchronization failure and the clock attacked by forgery, the synchronization error may be several μs. The detection error depends on the performance of the traveling wave detection method, the steepness of the traveling wave

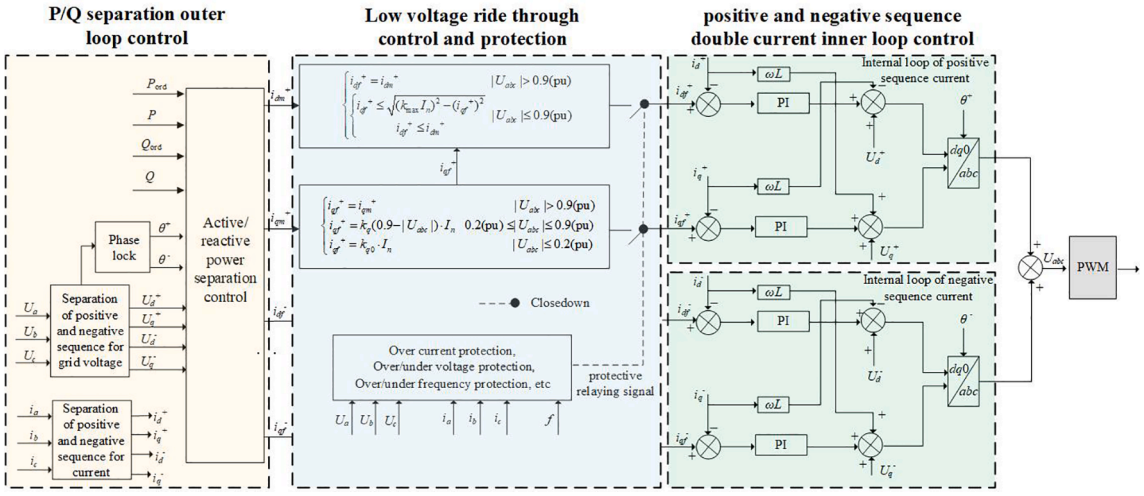

Fig. 8. The control system of the IIDG.

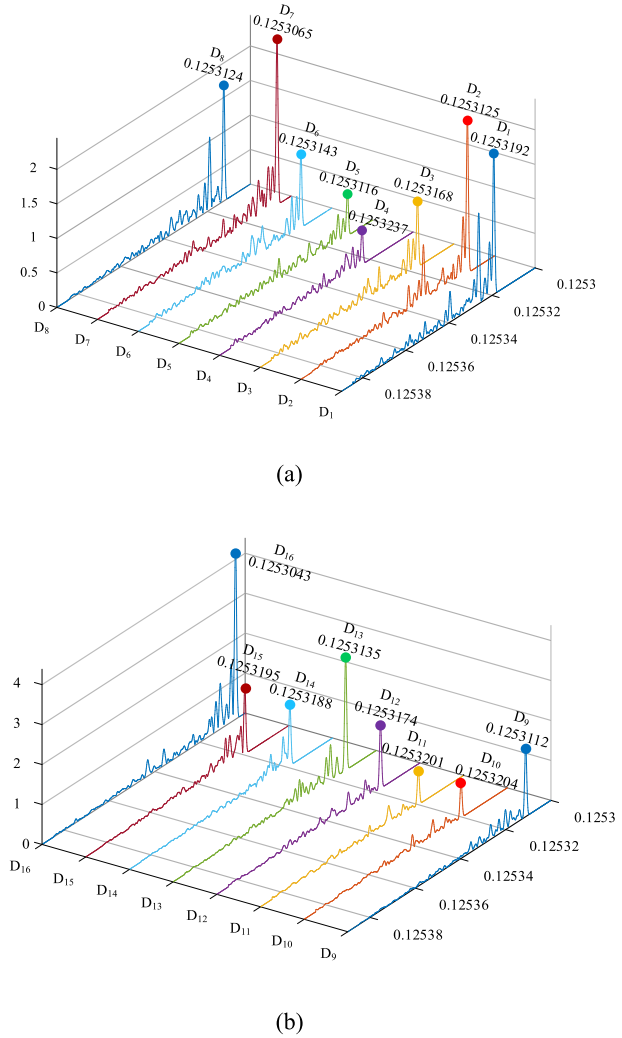

Fig. 9. The results of generalized S-transformation. (a) D-PMU $D_1 \sim D_8$. (b) D-PMU $D_9 \sim D_{16}$.

head, the transmission error of the sensor and the sampling rate of the measuring device. The performance of the existing traveling wave detection methods is relatively stable, and the detection error is

Table 3
The first arrival times of the traveling waves.

D-PMU	Arrival Time (s)	D-PMU	Arrival Time (s)
D_1	0.1253192	D_9	0.1253112
D_2	0.1253125	D_{10}	0.1253204
D_3	0.1253168	D_{11}	0.1253201
D_4	0.1253237	D_{12}	0.1253174
D_5	0.1253116	D_{13}	0.1253135
D_6	0.1253143	D_{14}	0.1253188
D_7	0.1253065	D_{15}	0.1253195
D_8	0.1253124	D_{16}	0.1253043

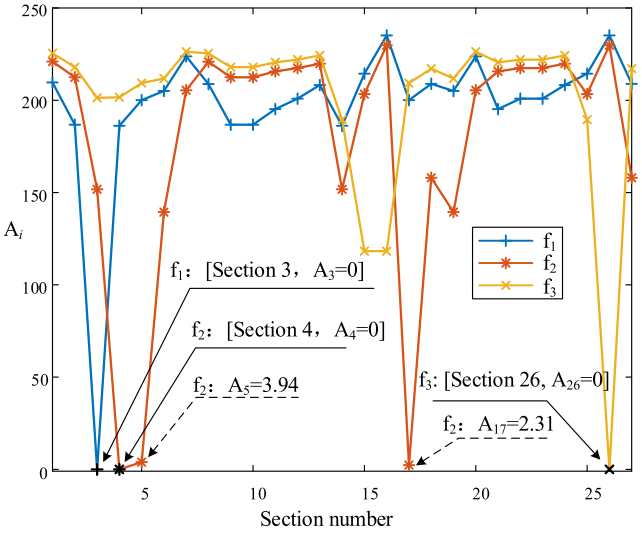

Fig. 10. The faulty section identification results of f_1, f_2 and f_3.

generally less than 2 sampling points. Considering the 10 MHz sampling rate adopted in this paper, the detection time error is set within ± 0.3 μs. Therefore, the robustness of the proposed method to time errors is verified in the following two cases: 1) only the synchronization errors exist, 2) both the detection errors and the synchronization errors exist.

1) Only the synchronization errors exist

Take the fault f_1 as an example, when the arrival time of detector D_1 has a synchronous error of 3 μs、6μs、9μs and 12 μs, the faulty section identification results are shown in Fig. 12, the clustering results of each case are shown in Fig. 13, and the fault location results and error

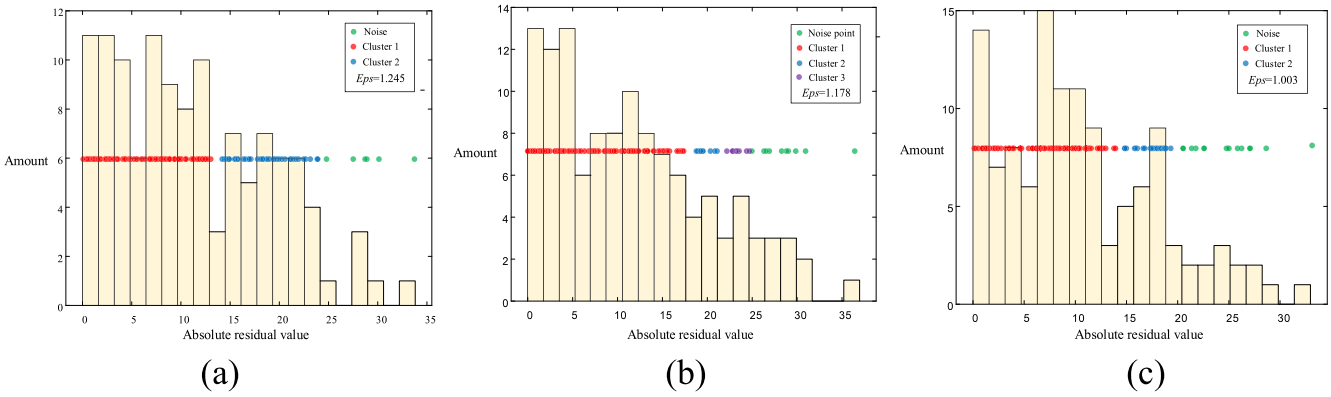

Fig. 11. The clustering results of f_1, f_2, f_3. (a) f_1. (b) f_2. (c) f_3.

Table 4
The fault location results and error analysis of f_1, f_2 and f_3.

fault	v (m/s)	l (m)	v' (m/s)	l' (m)	Initial error(m)	Corrected error (m)	Rate of error reduction
f_1	2.9732e + 8	1036.678	2.9763e + 8	1031.854	9.678	**3.454**	**64.31%**
f_2	2.9854e + 8	6.992	2.9840e + 8	5.784	8.992	**5.784**	**35.68%**
f_3	2.9949e + 8	91.078	2.9936e + 8	93.164	10.922	**6.836**	**37.41%**

Note: l and l' are the distance between the fault location result and B_3, B_4 or B_{11}, the ideal value is 3200 m, 0 m and 100 m respectively.

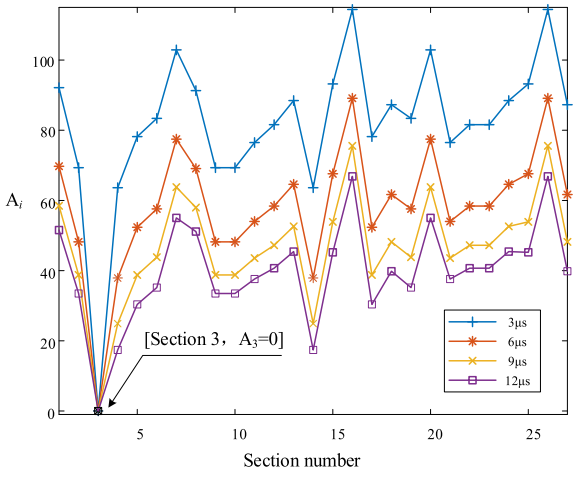

Fig. 12. The faulty section identification results when the arrival time of detector D_1 has a synchronous error of 3 μs、6μs、9μs and 12 μs.

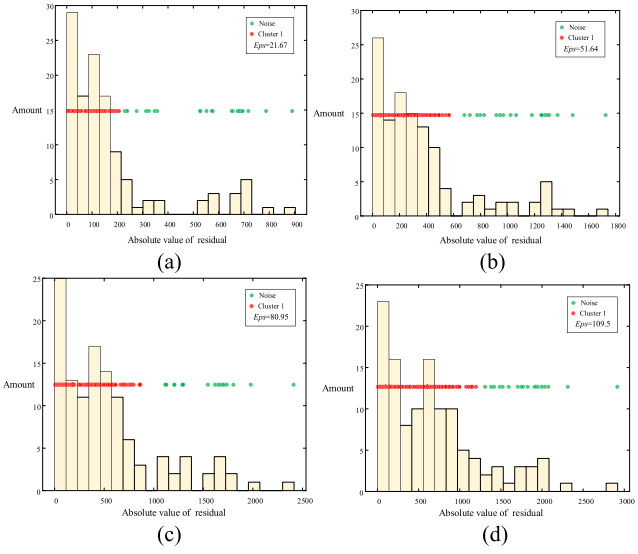

Fig. 13. The clustering results when the arrival time of detector D_1 has a synchronous error. (a) 3 μs. (b) 6 μs. (c) 9 μs. (d) 12 μs.

analysis are shown in Table 5.

Take the fault f_1 as an example, when the arrival times of several detectors have synchronization time errors, the following five cases are simulated and calculated. Case1: detectors D_1 and D_2 have a synchronous error of 2 μs. Case2: detectors D_1 and D_2 have a synchronous error of 4 μs. Case3: detectors D_1, D_2 and D_{13} have a synchronous error of 4 μs. Case4: detectors D_1, D_2 and D_{13} have a synchronous error of 6 μs. Case5: detectors D_1, D_2, D_{13} and D_{15} have a synchronous error of 6 μs. The faulty section identification results are shown in Fig. 14, the clustering results of each case are shown in the Appendix, and the fault location results and error analysis are shown in Table 6.

It can be analysed that when synchronization errors exist, the MSSE difference between the faulty section and the non-fault sections becomes smaller from Figs. 10, 12, 14. Even so, the MSSE of the faulty section is still significantly smaller than that of the non-fault sections, so the fault section can be correctly identified. It can be seen that the error of fault location after residual clustering has been greatly reduced, and the absolute error is less than 100 m which has high accuracy from Table 5, 6.

Table 5
The fault location results and error analysis when the arrival time of detector D_1 has a synchronous error.

Time error (μs)	l (m)	l' (m)	Initial error(m)	Corrected error (m)	Rate of error reduction
+3	945.369	1021.504	81.631	**5.496**	**93.27%**
+6	866.608	1021.504	160.392	**5.496**	**96.57%**
+10	794.609	1021.504	232.391	**5.496**	**97.64%**
+12	732.356	975.635	294.644	**51.365**	**82.65%**

Note: l and l' are the distance between the fault location result and B_3, the ideal value is 1027 m.

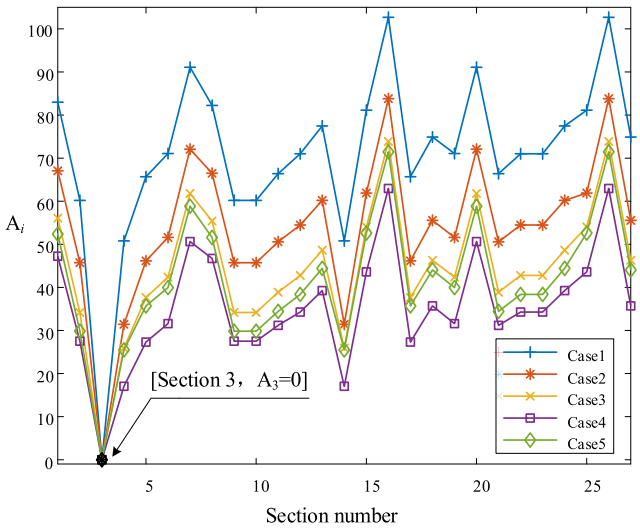

Fig. 14. The faulty section identification results when several detectors have synchronization time errors.

It is verified that the proposed method in this paper has strong robustness to synchronization time errors.

The results in Table 6 show that the detectors with synchronization errors in Case1 and Case2 are the same, but the magnitude of synchronization time errors are different. The time error of Case2 is greater than that of Case1, so the location error of Case2 is also greater than that of Case1, which is consistent with the common sense. Similarly, Case3 and Case4 also conform to this rule. It is worth noting that the synchronization time errors of Case2 and Case3 are equal, which are 4 μs, and the number of detectors with synchronization errors in Case3 increases D_{13} compared with Case2. Although the number of detectors with synchronization errors increases, the location error of Case3 decreases. The reason is that the faulty section (section B_2B_3) divides the entire network into two parts, as shown in Fig. 15. Detectors D_1 and D_2 belong to set $\boldsymbol{S}_\mathbf{u}$, while detector D_{13} belongs to set $\boldsymbol{S}_\mathbf{d}$, which are located in two different sets. The synchronization error of D_{13} has a certain offset effect on the synchronization errors of D_1 and D_2, which reduces the location error. Similarly, Case4 and Case5 also conform to this rule.

2) Both the detection errors and the synchronization errors exist.

Take the fault f_1 as an example, the random detection errors between −0.3 μs and 0.3 μs are applied to all detectors, and the additional synchronization errors are applied to few detectors. The specific time errors of all detectors are shown in Table 7. The faulty section identification results are shown in Fig. 16, the clustering results of each case are shown in the Appendix, and the fault location results and error analysis are shown in Table 8.

In Table 8, the absolute errors of fault location in all cases are less than 80 m. The location errors are greatly reduced after residual clustering, which can avoid the failure of fault location due to the time errors to a certain extent. The proposed method still has strong robustness to time errors when both the detection time errors and the synchronization time errors exist.

In the above analysis, the fault point f_1 is close to the substation B_3, about 1027 m. To verify the effectiveness of the proposed method when the fault is far away from the substation, the simulation analysis is performed on f_4. The fault f_4 is located on section 23 (section D_3B_8), 3200 m away from the branch point B_8, and 5963 m away from substation B_3. The applied synchronization time error is shown in Table 7. The faulty section identification results are shown in Fig. 17, and the fault location results and error analysis are shown in Table 9. It can be found that the absolute error of the location results in all cases are less than 90 m. Therefore, the proposed method can still work reliably when the fault is far from the substation.

4.4. The performance compared with the existing method

To further illustrate the advantages of the proposed method, the performance of the proposed method is compared with that of the multi-terminal traveling wave fault location method in [25]. The existing method constructs the location criterion by using the arrival time differences of traveling waves. First, the reference points are arranged every 20 m on the lines, then the fault simulation is carried out for all reference points to evaluate which reference point is closest to the actual fault location, so as to realize fault location.

The time errors shown in Table 7 are applied to all the detectors. The fault location results of the two methods are shown in Fig. 18. The average absolute errors of the two methods are 30.930 m and 112.830 m respectively. The fault location error of the method in this paper is reduced by 81.90 m and the location accuracy is improved by 72.59%. It can be seen that this method has the stronger tolerance to time errors.

5. Field test verification

In order to verify the performance of the proposed positioning method, the field artificial short-circuit tests were put into practice. The topological structure of the 10 kV test network is shown in Fig. 19 with a

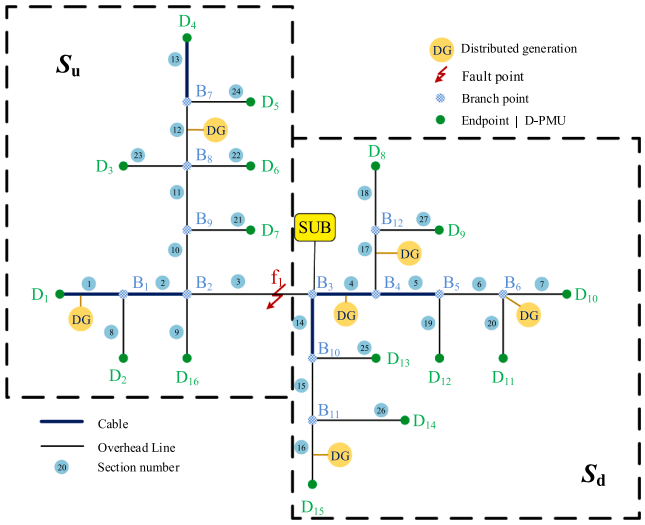

Fig. 15. The network divided result of the faulty section B_2B_3.

Table 6
The fault location results and error analysis when several detectors have synchronization time errors.

Case	Detector	Time error (μs)	l (m)	l' (m)	Initial error(m)	Corrected error (m)	Rate of error reduction
Case1	D_1、D_2	+2	940.276	1035.293	86.724	**8.293**	**90.44%**
Case2	D_1、D_2	+4	850.457	970.811	176.543	**56.189**	**68.17%**
Case3	D_1、D_2、D_{13}	+4	916.172	1012.597	110.828	**14.403**	**87.01%**
Case4	D_1、D_2、D_{13}	+6	842.747	933.936	184.253	**93.064**	**49.49%**
Case5	D_1、D_2、 D_{13}、D_{15}	+6	919.437	946.367	117.563	**76.633**	**34.82%**

Note: l and l' are the distance between the fault location result and B_3, the ideal value is 1027 m.

Table 7
The specific time errors of all detectors.

Case	D_1	D_2	D_3	D_4	D_5	D_6	D_7	D_8	D_9	D_{10}	D_{11}	D_{12}	D_{13}	D_{14}	D_{15}	D_{16}
Case1	**−3.1**	0	−0.3	−0.1	−0.2	+0.2	−0.1	0	−0.2	+0.1	−0.1	+0.3	+0.1	+0.1	0	−0.2
Case2	**+6.3**	+0.2	+0.1	0	+0.3	−0.1	+0.2	+0.2	−0.1	0	−0.3	−0.3	0	+0.2	+0.3	−0.2
Case3	**−2.2**	**−1.9**	−0.2	−0.1	−0.2	−0.2	+0.3	+0.3	0	−0.3	−0.2	−0.1	+0.2	−0.3	−0.3	−0.2
Case4	**+4.1**	**+4.3**	+0.2	−0.3	+0.3	+0.1	0	+0.1	−0.2	−0.2	+0.3	0	0	−0.2	+0.1	+0.1
Case5	**−4.0**	**−3.9**	+0.1	0	−0.2	0	−0.2	−0.3	+0.2	0	+0.3	+0.1	**−3.8**	+0.2	+0.2	+0.3
Case6	**+6.3**	**+6.1**	0	0	−0.2	+0.1	+0.2	+0.2	−0.1	−0.2	0	+0.1	**+5.7**	−0.2	**+6.1**	−0.3

Note: The units in tables are μs.

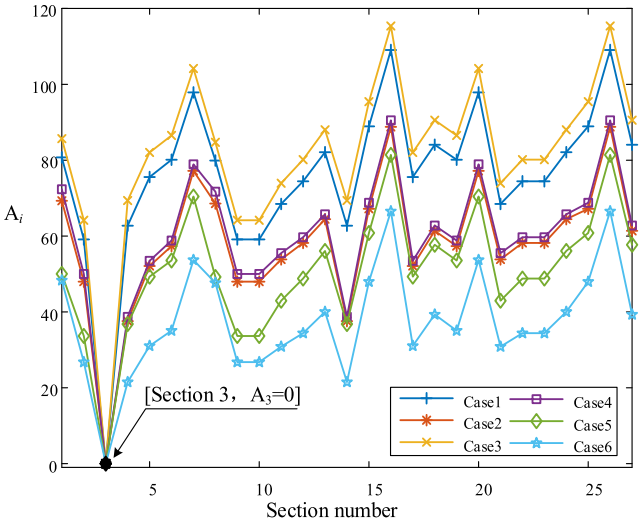

Fig. 16. The faulty section identification results when both the detection errors and the synchronization errors exist.

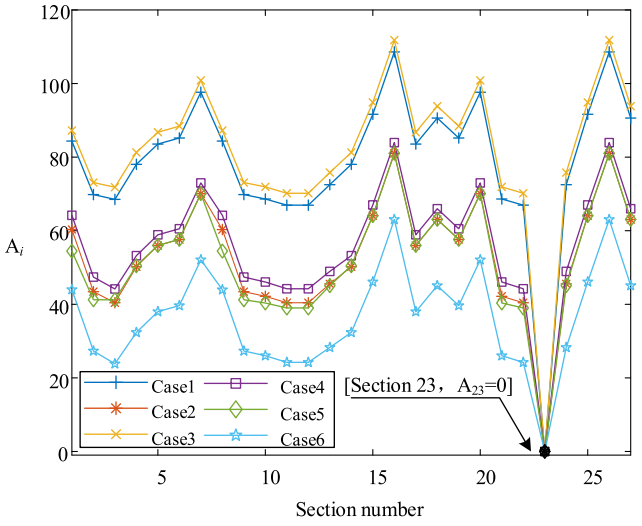

Fig. 17. The faulty section identification result for f_4 when both the detection errors and the synchronization errors exist.

Table 8
The fault location results and error analysis when both the detection errors and the synchronization errors exist.

Case	l (m)	l' (m)	Initial error(m)	Corrected error (m)	Rate of error reduction
1	1100.654	1034.135	73.654	**7.135**	**90.31%**
2	862.583	1016.844	164.417	**10.156**	**93.82%**
3	1102.407	1042.079	75.407	**15.079**	**80.00%**
4	843.430	998.437	183.570	**28.563**	**84.44%**
5	1065.861	1042.602	38.861	**15.602**	**59.85%**
6	917.324	949.513	119.676	**77.487**	**35.25%**

Note: l and l' are the distance between the fault location result and B_3, the ideal value is 1027 m.

Table 9
The fault location results and error analysis for f_4 when both the detection errors and the synchronization errors exist.

Case	l (m)	l' (m)	Initial error(m)	Corrected error (m)	Rate of error reduction
1	3163.661	3194.237	36.339	**5.763**	**84.14%**
2	3240.013	3213.952	40.013	**13.952**	**65.10%**
3	3244.345	3214.149	44.345	**14.149**	**68.09%**
4	3064.691	3165.145	135.309	**34.855**	**74.24%**
5	2881.119	3120.534	318.881	**79.466**	**75.08%**
6	2848.846	3112.774	351.154	**87.226**	**75.16%**

Note: l and l' are the distance between the fault location result and B_8, the ideal value is 3200 m.

total length of 23.635 km. Where the length of cable lines is 16.114 km and the length of overhead lines is 7.521 km.

The D-PMUs used in the field tests were provided by Changsha University of Science and Technology and Beijing Sifang Automation CO., LTD., [13,42,43]. The D-PMU and its installation are shown in Fig. 20. The arrival time of the travelling wave is collected locally by the travelling wave detection module sheathed on the ground line of the distribution transformer, as shown in Fig. 21. Rogowski coil is used to convert the current flowing through the grounding line into voltage wave signal. Furthermore, the wave head detection can be realized based on the change rate of wave head, the duration of wave head and the amplitude of wave head, and combined with the S transform or other time–frequency analysis algorithms. The sampling rate of this device can reach up to 20 MHz (10 MHz is used in the test). As the function extension module of D-PMU, the traveling wave module is embedded in D-PMU, which is only half of the mobile phone size. The clock timing adopts the complementary correction method of GPS/Beidou satellite clock and constant temperature crystal oscillator error. The synchronous clock error is about 10 ns, which has high sensitivity and accuracy of wave front detection.

When a fault occurs, each D-PMU transmits the recorded initial traveling wave arrival time T_i and the transformer number to the cloud computing platform of the background master station through the communication link (optical fiber / 4G). The cloud platform executes the optimization algorithm proposed in this paper to achieve accurate fault location. Finally, the fault location results are released through Web and SMS to remind operation and maintenance personnel to patrol and maintain according to the location result.

The unmanned aerial vehicle was used to create two interphase metal short-circuit fault faults, as shown in Fig. 22. The two faults are located on section 3, which are respectively 1502 m and 1501 m away from 1#Tower. The faulty section identification results are shown in Fig. 23, and the fault location results are shown in Table 10. It can be found that the two location errors are 70.303 m and 89.037 m from

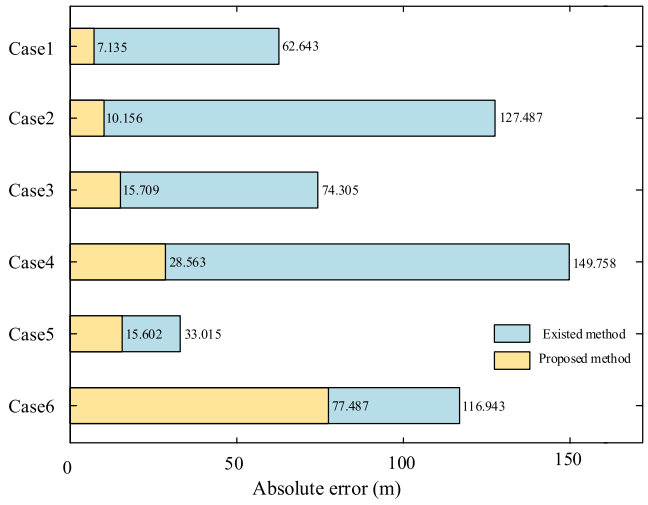

Fig. 18. The performance comparison between the proposed method and existing method.

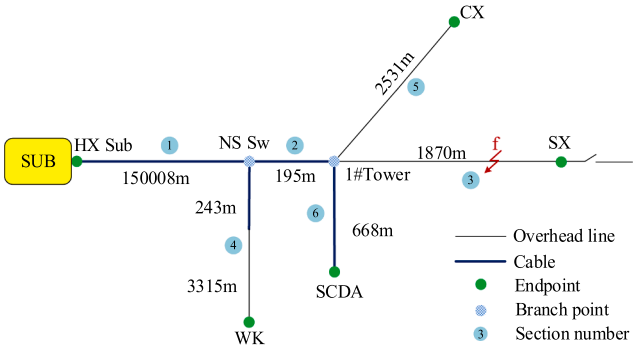

Fig. 19. The topology of the test network.

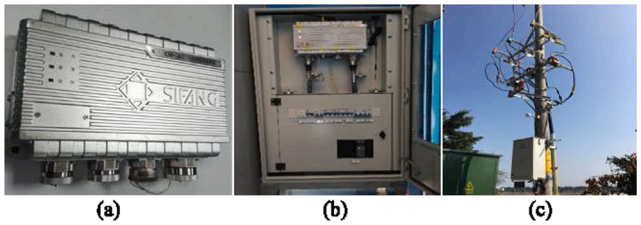

Fig. 20. D-PMU and its installation. (a) D-PMU housing. (b) (c) installation.

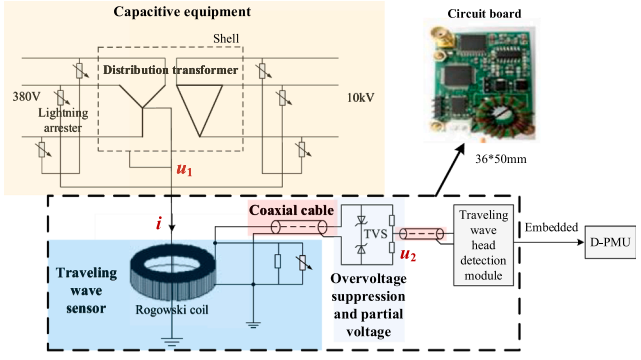

Fig. 21. The structure diagram of traveling wave detection module.

Fig. 22. The artificial short-circuit test.

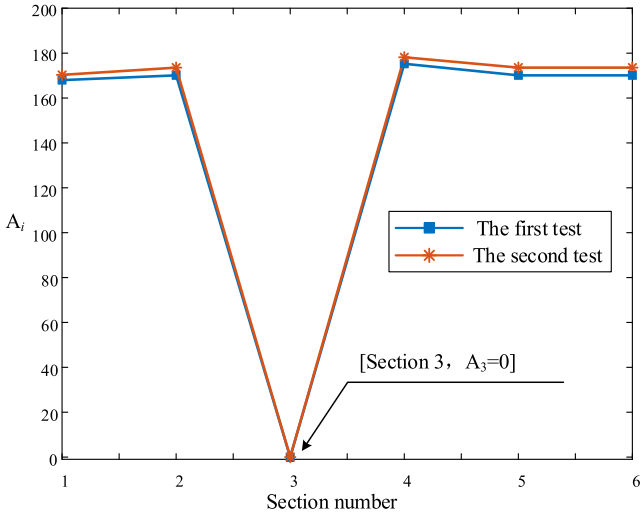

Fig. 23. The faulty section identification results.

Table 10
The fault location results of the field tests.

Actual fault location (m)	l (m)	l' (m)	Initial error(m)	Corrected error (m)	Rate of error reduction
1502	1382.621	1414.963	119.379	**87.037**	**27.09%**
1501	1407.328	1430.697	93.672	**70.303**	**25.77%**

Note: l and l' are the distance between the fault location result and 1#Tower, the ideal value is 1502 m and 1501 m respectively.

Table 10, while the location errors of simulation study in Section 4.2 are less than 20 m. There are three reasons for the larger location error of the field test:

(1) According to the sag effect [1], the length of overhead line which is affected by thermal expansion and cold contraction will change with the change of conductor temperature. In the field test, there may be errors between the actual line length and the recorded line length.
(2) Simulation study has limitations. On the one hand, the influence of sensors is not considered in the simulation modelling, including the specific influence of A/D conversion in the process of signal transmission, the range and accuracy of sensors on the traveling wave signal. On the other hand, although 30 dB Gaussian white noise is applied in the simulation, the

measurement noise in the actual test may not be strictly white noise which is more complex than the simulation environment.

(3) The field test is performed in a small distribution network, and the number of traveling wave detectors is small. The simulation study is performed in a large distribution network, and the number of traveling wave detectors is large. The residual clustering algorithm proposed in this paper is an unsupervised learning process based on a large number of data samples, which has advantages in large distribution networks. Therefore, the rate of location error reduction of the field test is less than that of the simulation study, and the location error of the field test is relatively large.

Although the location error of the field test is larger that of the simulation study, the location error is still less than 100 m, which can greatly shorten the range of manual patrol and still has great practical application value.

6. Conclusion

This paper proposes a multi-terminal traveling wave fault location method for active distribution network based on residual clustering. The following conclusions are obtained:

(1) The MSSE of each section is calculated by utilizing the PSO algorithm. Compared with the MSSE of all sections, the section with the minimum value is identified as the faulty section, and the initial solution the fault distance is obtained. In the above process, the wave velocity is taken as the unknown quantity, thus the location result is not affected by the error of wave velocity.

(2) DBSCAN algorithm is utilized to cluster the residuals of the faulty section to identify the bad data which are affected by time errors. The remained normal data are used to repeatedly construct the optimization model and calculate the corrected solution of the fault distance. It can greatly improve the accuracy of fault location and has a strong tolerance to time errors.

(3) Simulation and field tests show that the proposed method has high fault location accuracy and strong robustness to time errors. It can be effectively applied to the active distribution networks with good engineering application prospects.

In this paper, the proposed method is mainly used for the distribution networks with radiant structure, the improvement strategy for the distribution networks with ring structure remains to be further studied.

CRediT authorship contribution statement

Jian Qiao: Conceptualization, Data curation, Formal analysis, Investigation, Methodology, Validation, Writing - original draft, Writing - review & editing. **Xianggen Yin:** Conceptualization, Funding acquisition, Methodology, Resources. **Yikai Wang:** Conceptualization, Formal analysis, Investigation, Methodology, Writing - original draft, Writing - review & editing. **Wen Xu:** Data curation, Validation. **Liming Tan:** Formal analysis, Validation.

Declaration of Competing Interest

The authors declare that they have no known competing financial interests or personal relationships that could have appeared to influence the work reported in this paper.

Acknowledgments

This work is supported by the National Key Research and Development Program of China (2017YFB0902900, 2017YFB0902903), the National Natural Science Foundation of China (51877089). The authors thank the reviewers for their invaluable suggestions.

Appendix A. Supplementary data

Supplementary data to this article can be found online at https://doi.org/10.1016/j.ijepes.2021.107070.

References

[1] Cesar G, Ali A. Fault location in active distribution networks containing distributed energy resources (DERs). IEEE Trans Power Deliv (Early Access).
[2] Jia Q, Dong XZ, Mirsaeidi S. A traveling-wave-based line protection strategy against single-line-to-ground faults in active distribution networks. Int J Electrical Power Energy Syst 2018;107:403–11.
[3] Aftab MA, Hussain SMS, Ali I, Ustun TS. Dynamic protection of power systems with high penetration of renewables: a review of the traveling wave based fault location techniques. Int J Electrical Power Energy Syst 2020;114..
[4] Daisy M, Dashti R. Single phase fault location in electrical distribution feeder using hybrid method. Energy 2016;133:356–68.
[5] Ji L, Tao XJ, Fu Y. A new single ended fault location method for transmission lime based on positive sequence superimposed network during auto-reclosing. IEEE Trans Power Deliv 2019;34(3):1019–29.
[6] Dashti R, Sadeh J. Fault section estimation in power distribution network using impedance-based fault distance calculation and frequency spectrum analysis. IET Gener Transm Distrib 2014;8(8):1406–17.
[7] Seyed HM, Mohamad HJ, Ebadollah K. Robust wide area fault location considering network parameters error. IEEE Trans Power Deliv 2019;34(3):786–94.
[8] Xi YH, Li ZW, Zeng XJ. Fault location based on travelling wave identification using an adaptive extended Kalman filter. IET Gener Transm Distrib 2018;12(6):1314–22.
[9] Eleonora RS, Vincenzo LV, Antonio DS. A Two-End Traveling Wave Fault Location System for MV Cables. IEEE Trans Ind Appl 2019;55(2):1180–8.
[10] Izykowski J, Rosolowski E, Balcerek P. Accurate noniterative fault location algorithm utilizing two-end unsynchronized measurements. IEEE Trans Power Deliv 2010;25(1):72–80.
[11] IEEE Trans Power Deliv 2016;31(5):2296–8.
[12] Deng F, Zeng XJ, Mao Y, Zu YR, Me LJ. A novel multi-terminal fault location method based on traveling wave time difference for active distribution network. 25th IEEE ICAC. 2019:387–92.
[13] Deng F, Zu YR, Mao Y, Zeng XJ, Li ZW. A method for distribution network line selection and fault location based on a hierarchical fault monitoring and control system. Int J Electrical Power Energy Syst 2020;123..
[14] Usman MU, Faruque MO. Validation of a PMU-based fault location identification method for smart distribution network with photovoltaics using real-time data. IET Gener Transm Distrib 2018;12(21):5824–33.
[15] Moslem S, Farhad N. Fault location on branched networks using mathematical morphology. IET Gener Transm Distrib 2018;12(1):207–16.
[16] Xie LW, Luo LF, Li Y, Zhang Y, Cao YJ. A traveling wave-based fault location method employing VMD-TEO for distribution network. IEEE Trans Power Deliv 2019;35(4):1987–98.
[17] Deng F, Li X, Zeng XJ, Li ZW. A novel multi-terminal fault location method based on traveling wave time difference for radial distribution systems with distributed generators. Proc CSEE 2018;38(15):4399–409.
[18] Ning Y, Wang DZ, Li YL. Location of faulty section and faults in hybrid multi-terminal lines based on traveling wave method. Energies 2018;11:1105–23.
[19] Wang DZ, Ning Y, Zhang CL. An effective ground fault location scheme using unsynchronized data for multi-terminal lines. Energies 2018;11:2957–73.
[20] Ding JL, Wang X, Zheng YH. Distributed traveling-wave-based fault-location algorithm embedded in multiterminal transmission lines. IEEE Trans Power Deliv 2018;33(6):3045–54.
[21] Hanif L, Yaman EC. A machine learning and wavelet-based fault location method for hybrid transmission lines. IEEE Trans Smart Grid 2014;5(1):51–9.
[22] Cao PL, Shu HC, Yang B. Seeped-up robust features based single-ended traveling wave fault location: a practical case study in yunnan power grid of China. IET Gener Transm Distrib 2018;12(4):886–94.
[23] Shi SX, Zhu BE, Lei AY, Dong XZ. Fault location for radial distribution network via topology and reclosure-generating traveling waves. IEEE Trans Smart Grid 2019;10(6):6404–13.
[24] Robson S, Haddad A, Griffiths H. Fault location on branched networks using a multiended approach. IEEE Trans Power Deliv 2014;29(4):1955–63.
[25] Chen R, Yin X, X. Li YY, Lin JY. Computational fault time difference-based fault location method for branched power distribution networks. IEEE Access 2019;7:181972-82.
[26] Chen Y, Liu D, Xu BY. Wide-area traveling wave fault location system based on ice61850. IEEE Trans Smart Grid 2013;4(2):1207–15.
[27] Costa FB, Souza BA, Brito NSD. Real-time detection of fault-induced transient in transmission lines. IET Electron. Lett 2010;46:753–5.
[28] Wang D, Hou MQ. Travelling wave fault location algorithm for LCC-MMC-MTDC hybrid transmission system based on Hilbert-Huang transform. Int J Electrical Power Energy Syst 2020;121..
[29] Shafiullah MD, Abido MA. S-transform based FFNN approach for distribution grids fault detection and classification. IEEE Access 2018;6:8080–8.

[30] Sahoo B, Samantaray SR. An enhanced fault detection and location estimation method for TCSC compensated line connecting wind farm. Int J Electrical Power Energy Syst 2018;96:432–41.
[31] Wang L, Liu H, Dai LV, Liu Y. Novel method for identifying fault location of mixed lines. Energies 2018;11(6):1–19.
[32] Li XY, Dysko A, Burt GM. Traveling wave-based protection scheme for inverter-dominated microgrid using mathematical morphology. IEEE Trans Smart Grid 2014;5(5):2211–8.
[33] Liu NH, Gao JH, Zhang B, Wang Q. Self-adaptive generalized S-Transform and its application in seismic time-frequency analysis. IEEE Trans Geosci Remote 2019;57 (10):7849–59.
[34] Kong XY, Xu Y, Jiao ZB, Don DL, Yuan XX. Fault location technology for power system based on information about the power internet of things. IEEE Trans Ind Inform 2020;16(10):6682–92.
[35] Yu L, Jiao ZB, Wang XP, Chen W, Deng F. Accurate fault location scheme and key technology of medium-voltage distribution network with synchrophasor measurement units. Auto Electric Power Syst 2020;44(18):30–8.
[36] Ramesh L, Chakraborthy N, Chowdhury SP. Intelligent DE algorithm for measurement location and PSO for bus voltage estimation in power distribution system. Int J Electrical Power Energy Syst 2012;39(1):1–8.
[37] Huang HM, Liu F, Zha XM. Robust bad data detection method for microgrid using improved ELM and DBSCAN algorithm. J Energy Eng 2018;144(3):04018026.
[38] Cui B, Srivastava AK, Banerjee P. Synchrophasor-based condition monitoring of instrument transformers using clustering approach. IEEE Trans Smart Grid 2020;11 (3):2688–98.
[39] Zhou MZ, Wang YH, Srivastava AK. Ensemble-based algorithm for synchrophasor data anomaly detection. IEEE Trans Smart Grid 2019;10(3):2978–88.
[40] Katter M, Ustuner K, Blank R. Model for calculating J(H) curves of Ni coated Nd-Fe-B magnets. J Iron Steel Res Int 2006;13:87–91.
[41] Ning Y, Wang DZ, Li YL, Zhang HX. Location of faulty section and faults in hybrid multi-terminal lines based on traveling wave method. Energies 2018;11:1105–23.
[42] Deng F, Li P, Zeng XJ, Yu L. Fault Line Selection and Location Method Based on Synchrophasor Measurement Unit for Distribution Network. Automation of Electric Power Syst 2020;44(19):160–71.
[43] Yu L, Jiao ZB, Wang XP, Chen W. Accurate Fault Location Scheme and Key Technology of Medium-voltage Distribution Network with Synchrophasor Measurement Units. Automation of Electric Power Syst 2020;44(18):30–8.

Jian Qiao was born in Liaoning, China, in 1997. He received the B.S. degree from Huazhong University of Science and Technology (HUST), Wuhan, China, in 2019. He is currently pursuing the Ph.D. degree in electrical engineering at HUST, major in power system protection and control.

Xianggen Yin was born in 1954. He received the Ph.D. degree in electrical engineering from Huazhong University of Science and Technology (HUST), Wuhan, China, in 1989. Currently, he is a Professor at HUST. His research areas include protective relaying and power system stability control.

Yikai Wang was born in Liaoning, China, in 1996. He received the B.S. degree from North China Electric Power University, Baoding, China, in 2018. He is currently working toward the Ph.D. degree in electrical engineering at Huazhong University of Science and Technology, major in power system protection and control.

Wen Xu was born in Hainan, China, in 1998. She received the B.S. degree from Tsinghua University, Beijing, China, in 2019. She is currently working toward the M.Sc. degree in electrical engineering at Huazhong University of Science and Technology, major in power system protection and control.

Liming Tan was born in Hunan, China, in 1998. He received the B.S. degree from Huazhong University of Science and Technology (HUST), Wuhan, China, in 2020. He is currently working toward the M.Sc. degree in electrical engineering at HUST, major in power system protection and control.